Preprint typeset using LaTeX style emulateapj v. 08/22/09

arXiv:1401.3287v1 [astro-ph.GA] 14 Jan 2014

STAR FORMATION RELATIONS IN NEARBY MOLECULAR CLOUDS

Neal J. Evans II, Amanda Heiderman, Nalin Vutisalchavakul
The University of Texas at Austin, Department of Astronomy, 2515 Speedway, Stop C1400, Austin, TX 78712-1205, USA

ABSTRACT

We test some ideas for star formation relations against data on local molecular clouds. On a cloud by cloud basis, the relation between the surface density of star formation rate and surface density of gas divided by a free-fall time, calculated from the mean cloud density, shows no significant correlation. If a crossing time is substituted for the free-fall time, there is even less correlation. Within a cloud, the star formation rate volume and surface densities increase rapidly with the corresponding gas densities, faster than predicted by models using the free-fall time defined from the local density. A model in which the star formation rate depends linearly on the mass of gas above a visual extinction of 8 mag describes the data on these clouds, with very low dispersion. The data on regions of very massive star formation, with improved star formation rates based on free-free emission from ionized gas, also agree with this linear relation.

Subject headings: star formation, galaxies, Milky Way

1. INTRODUCTION

The factors controlling star formation play an important role in understanding the formation and evolution of galaxies. Galaxy-scale studies have led to a number of empirical relations (Kennicutt 1998; Bigiel et al. 2008; Gao & Solomon 2004; Wu et al. 2005) and theoretical or semi-empirical explanations for these relations (for a nice review of ideas, see Leroy et al. 2008). Most of these observational and theoretical efforts did not consider data from studies of star formation in our own Galaxy, for which very detailed studies of star formation processes are available. Recently, there have been attempts to bring these two fields into closer communication, as reviewed by Kennicutt and Evans (2012). In doing so, one must be aware of significant differences and biases, but the rewards could be substantial.

We use detailed data on the gas and star formation properties of a sample of nearby ($d < 500$ pc, with one exception at 950 pc) clouds to test a number of suggestions for star formation relations. These clouds have the virtue of having very complete information, obtained in uniform ways, on their masses and star formation rates, including resolved studies of these properties across the face of the clouds. They are the only clouds for which such detailed studies are available over the whole cloud. On the other hand, these clouds may not be typical of those in the inner part of the Galaxy, which may be more characteristic of the regions generally studied in other galaxies (e.g., Longmore et al. 2013; Kruijssen et al. 2013).

To put the solar neighborhood in context, we note that the Sun lies in a part of the Galactic disk in which the gas surface density is dominated by atomic gas ($\Sigma_{\rm atomic} \sim 10$ $M_\odot$ pc^{-2}), while the smoothed out surface density of molecular gas is much less ($\Sigma_{mol} \sim 1$ $M_\odot$ pc^{-2}) (Dame et al. 2001, Nakanishi and Sofue 2006). The star formation rate surface density, Σ(SFR) ~ 3 $M_\odot$ pc^{-2}Gyr^{-1}, or 3×10^{-3} $M_\odot$ yr^{-1} kpc^{-2} (Misiriotis 2006). This Σ(SFR) is much lower than in the inner parts of the Galaxy or in many regions studied in other galaxies, but it is close to the average value over the inner 13.5 kpc of the Galaxy (Kennicutt and Evans 2012).

Electronic address: nje@astro.as.utexas.edu

1.1. *The Sample*

The clouds studied here are those from the c2d (Evans et al. 2003, 2009) and Gould Belt (Dunham et al. 2013, Allen et al. in prep.) Spitzer legacy programs. Depending on how they are divided, there are 18-29 clouds in the sample. In the version we use, there are 29 clouds because we separate clouds that were mapped separately with their own distances, sizes, and velocity dispersions. These clouds were mapped down to relatively uniform extinction levels ($A_V = 2$ mag, except in confused regions) in all the Spitzer bands from 3.6 to 160 μm. They are also targeted in Herschel surveys covering 60 to 500 μm (André et al. 2011), and some have been studied in more detail in millimeter continuum emission (e.g., Enoch et al. 2009) and molecular lines (e.g., Ridge et al. 2006). The properties used in this paper are shown for all 29 clouds in Table 1, along with median, mean, and standard deviation of the sample. The size is the effective radius ($r = \sqrt{A/\pi}$), $\dot{M}_*$ is the star formation rate, $M_{\rm cloud}$ is the cloud mass, generally measured down to $A_V = 2$ mag, $M_{\rm dense}$ is the mass above an extinction contour of $A_V = 8$ mag, Σ(SFR) is the surface density of the star formation rate, $\Sigma_{\rm gas}$ is the gas surface density averaged over the whole cloud, $t_{\rm ff}$ is the free-fall time calculated from the mean cloud volume density, Δv is the mean linewidth (see Appendix for details), and $t_{\rm cross} = 2r/\langle v \rangle$ is the crossing time for the cloud. For the clouds as a whole, the median, mean, and standard deviation for the depletion time ($t_{\rm dep} = M_{\rm cloud}/\dot{M}_*$) are 106, 201, and 240 Myr, and for the "efficiency" per free-fall time ($\epsilon_{\rm ff} = t_{\rm ff}/t_{\rm dep}$) are 0.016, 0.018, and 0.013. For the "dense" gas (above the contour of $A_V = 8$ mag), the median, mean, and standard deviation for $t_{\rm ff}$ are 0.53, 0.71, and 0.38 Myr, for $t_{\rm dep}$ are 45, 47, and 24 Myr, and for $\epsilon_{\rm ff}$ are 0.019, 0.018, and 0.008. These values consider the 14 clouds with $M_{\rm dense} > 0$ and $\dot{M}_* > 0$.

For this paper, we focus on the gas properties, especially surface and mean volume densities, derived from extinction maps, and star formation rates, based on

counting young stellar objects (YSOs) identified by their infrared excess. The basic methods for determining these quantities were described for the c2d clouds in Evans et al. (2009) and Heiderman et al. (2010), and the same techniques were used for the clouds studied in the Gould Belt project, so we give only a brief summary here.

The Spitzer surveys identified a large fraction of detected sources as background stars (2×10^4 to 1×10^5 per cloud for the c2d clouds). Extinctions were determined for each background star by fitting SEDs to the Spitzer and 2MASS photometry, with stellar photospheric models from the SSC tool, "Star-Pet," and the extinction law for $R_V = 5.5$ of Weingartner & Draine (2001), which matches multi-wavelength data well for these clouds (Chapman et al. 2009). The extinctions to individual stars were averaged over a Gaussian beam to make extinction and uncertainty maps, based on beam averaging the uncertainties in the individual extinctions. These maps allow us to probe extinctions up to $A_V \sim 40$ mag. We use maps with angular resolution of $270''$ for all clouds, corresponding to 0.34 pc at the mean distances of the clouds (256 pc). For further details, see Evans (2007) and updates in Heiderman et al. (2010). The extinction maps were used to calculate the mean extinction within extinction contours and the uncertainty in that mean propagated from the uncertainty maps. These averages were used to determine mass surface densities in contours of extinction, from which mean volume densities and total masses could be calculated. We follow the procedures used by Heiderman et al. (2010) in this paper. For conversion to mass surface density, we use Case A models for $R_V = 5.5$ dust, given by Weingartner & Draine (2001)[1]. The systematic uncertainties in this conversion are discussed in the Appendix.

The star formation rates were determined from counting YSOs, multiplying by the mean mass of stars and dividing by the relevant timescale. The identification of YSOs required careful discrimination against background stars and galaxies. Star-forming galaxies were the most problematic source of contaminants. A combination of color-color and color-magnitude diagrams using both Spitzer and 2MASS data were used to reject contaminants. For background galaxies, the SWIRE fields, artifically extincted to match the extinction for each cloud, were used to characterize the properties of galaxies in these diagrams. A weighted average over many criteria, optimized to remove both stars and galaxies, was adopted, and then examination by eye was used to remove remaining suspicious objects (about 8%). For clouds at low Galactic latitude (e.g., Serpens), background giants were a further ($\sim 7\%$) source of contamination, and these were removed when spectroscopy was available (Oliveira et al. 2009). For clouds farther from the plane, contamination was less than 5% (Spezzi et al. 2008). The detailed descriptions of this process are in Harvey et al. 2007; Evans 2007; Evans et al. 2009. There is an inevitable trade-off between minimizing contamination and maximizing completeness. The "official" products for c2d (Evans et al. 2009) and Gould Belt (Dunham et al. 2013) projects emphasized minimizing contamination. Recently Hsieh & Lai (2013) have reanalyzed the c2d clouds using still more color and magnitude criteria, and they find about $\sim 30\%$ more YSOs. If these newer techniques prove reliable, the star formation rates would increase by about 30%.

To convert numbers of YSOs to mass of forming stars, we used $\langle M_\star \rangle = 0.5$ M$_\odot$, based on a fully sampled initial mass function (Kroupa 2002; Chabrier 2003; Ninkovic & Trajkovska 2006), consistent with observations of at least one of our clouds; Spezzi et al. (2008) found $\langle M_\star \rangle = 0.52 \pm 0.11$ M$_\odot$ in Cha II.

To get the relevant timescales, the YSOs were classified into standard SED classes, Class I, Flat SED, Class II, and Class III, using spectral indices determined from all available photometry from 2 to 24 μm. Further distinction of Class 0 sources within the larger category of Class I sources used the bolometric temperature. The timescale relevant to each class was determined by the number in each class relative to the number of Class II sources, for which a timescale of 2 Myr was assumed. For tests on scales of the full cloud, we use all YSOs. For tests on smaller scales, we want to focus on objects that are still associated with their natal material; for these, we use only the Class I objects, with a timescale of 0.55 Myr, a slight update from the value in Evans et al. (2009), based on the full c2d plus Gould Belt sample. All references to Class I objects in this paper *include* Class 0 sources as well because the spectral index does not distinguish them.

The low luminosity objects in Classes I and Flat were most easily confused with extragalactic objects, especially for regions of low YSO surface density. Edge-on disks or Class II objects behind unusally high extinction regions were less common sources of contamination of the early classes. Heiderman et al. (2010) removed some of these objects from the sample by requiring detection of the $J = 3 \rightarrow 2$ line of HCO$^+$, which traces relatively high densities, following the findings of van Kempen et al. (2009). Surveys for HCO$^+$ toward all Class I and Flat SED objects in the full c2d and Gould Belt surveys have continued (Heiderman et al. in prep) but have not been completed. Based on the results so far, which were focused on regions of low extinction, the number of contaminants is not so large as to affect the Class I lifetimes significantly, but the fraction of contaminants in regions of low YSO surface density is about 50%. The fraction of Flat SED sources lacking HCO$^+$ emission was much higher, 74% (Heiderman et al. 2010). Since the Flat SED sources were less clearly associated with their natal material from the start, we consider only the Class I sources when we focus on smaller scales. Note that decreasing the number of Class I sources relative to the total would decrease their timescale, leaving the the star formation rate from Class I sources essentially unchanged.

The latest version of the YSO sample for the c2d and Gould Belt surveys (Dunham et al. 2013). has been used here. The sample contains 2966 YSO candidates, of which 367 are classified as Class I sources. Dunham et al. (2013) further restricted the sample of "protostars" by requiring data at submillimeter wavelengths, resulting in a sample of 230 objects. While such data was important for getting a luminosity distribution, the goal of Dunham et al. (2013), we do not require it here since we only wish to count Class I sources.

[1] See `http://www.astro.princeton.edu/$\sim$draine/dust/dust.html` for updates

2. MODELS FOR STAR FORMATION RELATIONS

2.1. *Empirical Relations*

The most well known star formation relation on the scale of whole galaxies is the Kennicutt-Schmidt relation (Schmidt 1959, 1963; Kennicutt 1998):

$$\Sigma(\mathrm{SFR}) = A\,\Sigma^{N}{}_{gas} \tag{1}$$

where $\Sigma_{\rm gas} = \Sigma_{\rm HI} + \Sigma_{\rm H_2}$ is the total gas density from H I and CO observations, but without correction for helium. Kennicutt (1998) found a best fit with $N = 1.4\pm0.15$. Inclusion of more galaxies and a wider range of galaxy types has not changed this result (Kennicutt & Evans 2012). Studies of the radial distribution of star formation within galaxies have found a similar relation between surface densities, but with more variation in the best fit for N. In addition, a threshold below which Σ(SFR) decreases rapidly is found around $\Sigma_{\rm gas} = 10\ \mathrm{M_\odot\ pc^{-2}}$ (Bigiel et al. 2008; Leroy et al. 2013); this threshold is associated with the transition between atomic and molecular-dominated ISMs. When only molecular gas is considered, the values of N tend to be smaller ($N = 1.0 - 1.4$). Large studies found $N = 1.0\pm0.2$ for the radial distributions of star formation and molecular gas surface densities (Bigiel et al. 2008; Leroy et al. 2013). The strong, linear correlation with molecular gas has been extended to the outer regions of galaxies by a line stacking analysis of CO observations (Schruba et al. 2011). That analysis agrees with data in the outer Galaxy that shows star formation inevitably associated with molecular gas, even in that very atomic-dominated part of the Galaxy (Snell et al. 2002). These studies are in clear accord that the molecular gas is most clearly associated with star formation. However, issues of the conversion of CO observations into molecular column density, especially for lower metallicity galaxies, introduce significant uncertainties (Kennicutt & Evans 2012; Bolatto et al. 2013). Since we compare to data in our Galaxy, our conclusions need not apply for very different metallicities.

Another relation that applies to whole galaxies was derived from studies of HCN emission (mostly $J = 1 \rightarrow 0$), which traces denser gas than does CO (Solomon & Sage 1988; Gao & Solomon 2004; Wu et al. 2005). These studies demonstrated a linear relation between total star formation rate and total mass of dense gas, as estimated from HCN:

$$\dot{M}_*(\mathrm{M_\odot\ yr^{-1}}) \sim 1.2\times10^{-8} M_{\rm dense}(\mathrm{M_\odot}), \tag{2}$$

where we have taken the specific relation from Wu et al. (2005). This relation had a smaller dispersion than the relation with total gas or even molecular gas. This relation was consistent with many studies of star formation in the Galaxy showing that star formation was highly correlated with relatively dense gas within the molecular cloud (Onishi et al. 1998; Enoch et al. 2007; Johnstone et al. 2004; André et al. 2010; Li et al. 1997; Lada 1992).

2.2. *Semi-empirical Models*

These empirical relations have motivated two apparently conflicting models. In one, the whole galaxy KS relation is propagated into a "universal local" relation between volume densities (Krumholz et al. 2012):

$$\rho(\mathrm{SFR}) \propto {\rho_{\rm gas}}^{x} \tag{3}$$

The idea is that the amount of gas divided by the free fall time should be reflected in the star formation rate, and $t_{\rm ff} \propto \rho^{-0.5}$ leading to $x = 1.5$, equal within uncertainties to the exponent in the KS relation (Krumholz & McKee 2005; Krumholz & Thompson 2007; Narayanan et al. 2008). In more definite form, the theoretical relation is given by

$$\rho(\mathrm{SFR}) = f_{\rm H_2}\epsilon_{\rm ff}\rho_{\rm gas}/t_{\rm ff}, \tag{4}$$

where $f_{\rm H_2}$ is the fraction of the mass in molecular form and $\epsilon_{\rm ff}$ is the "efficiency" per free-fall time ($t_{\rm ff}$) (equation 1 of Krumholz et al. 2012). Since we focus on molecular gas, we set $f_{\rm H_2} = 1$. With

$$t_{\rm ff} = \sqrt{3\pi/32G\rho_{\rm gas}} = 8.08\mathrm{Myr}{\rho_{\rm gas}}^{-0.5}(\mathrm{M_\odot pc^{-3}}), \tag{5}$$

we have in cgs units

$$\rho(\mathrm{SFR}) = 4.76\times10^{-4}\epsilon_{\rm ff}{\rho_{\rm gas}}^{1.5} \tag{6}$$

or, in more convenient units

$$\rho(\mathrm{SFR})(\mathrm{M_\odot Myr^{-1}pc^{-3}}) = 0.12\epsilon_{\rm ff}{\rho_{\rm gas}}^{1.5}(\mathrm{M_\odot pc^{-3}}) \tag{7}$$

For comparison to data, we take $\epsilon_{\rm ff} = 0.01$ (Krumholz and McKee 2005).

The other model builds on the observations of density thresholds in nearby clouds (Heiderman et al. 2010; Lada et al. 2010) to argue that the star formation rate is linearly proportional to the mass of gas above a surface density or volume density threshold. Based on studies of nearby clouds, Lada et al. (2012) suggest the following relation:

$$\dot{M}_*(\mathrm{M_\odot\ yr^{-1}}) = 4.6\times10^{-8} f_{\rm dense} M_{\rm mol}(\mathrm{M_\odot}) \tag{8}$$

or

$$\dot{M}_*(\mathrm{M_\odot\ Myr^{-1}}) = 0.046 M_{\rm dense}(\mathrm{M_\odot}) \tag{9}$$

It would reproduce the relation with dense gas seen in high-mass star forming regions in the MW (equation 2) if the conversion from far-infrared luminosity to star formation rate is scaled up by a factor of 3.8. Alternatively, the relation between dense gas as measured by extinction versus HCN $J = 1 \rightarrow 0$ luminosity could be adjusted.

While these two models agree that star formation is strongly concentrated in denser gas, they differ in detail. Lada et al. (2012) have argued that their scaling law can be compatible with a volumetric law only if $x = 1$ and $\rho_{\rm gas} > \rho_{\rm th}$, where $\rho_{\rm th}$ is a threshold volume density that corresponds on average to the surface density threshold.

Other models have also been suggested, mostly involving timescales different from the free-fall time. On a galactic scale, the orbital time ($t_{\rm orb}$) could be relevant, and various studies have found good correlations between Σ(SFR) and $\Sigma_{\rm gas}/t_{\rm orb}$ (Kennicutt 1998). This relation may also be useful for understanding starburst galaxies (Daddi et al. 2010; Genzel et al. 2010), but it cannot be extended to the level of molecular clouds in the MW (e.g., Krumholz et al. 2012).

A possibly more relevant timescale for individual clouds or clumps is the crossing time ($t_{\rm cross}$), defined by

the size of a relevant dimension divided by an appropriate speed, which could be the thermal sound speed or, more likely, the turbulent mean speed (Elmegreen 2000).

3. TESTS OF MODELS

3.1. *Uncertainties*

The uncertainties used in this section can be divided into two types, which are discussed in much more detail in the Appendix. The first type is an observational uncertainty which may vary from cloud to cloud or from region to region. These would affect the correlation coefficients and the slope of linear fits, so they are included in figures and fits. The second type of uncertainty is a systematic uncertainty, which affects all the clouds and regions in the same way. These are not included on the individual points in the plots nor in the fits, but they are shown separately in some plots.

3.2. *Tests of the free-fall model*

First, we test the pure form of the volumetric star formation model (equation 7) by plotting ρ(SFR) versus $\rho_{\rm gas}$ for the regions of increasing surface density in nearby clouds. To do so, we convert the surface densities of both gas and star formation rate into volume densities by dividing by a length scale. Without further information on the depth of the cloud, we assume a set of nested spherical shells with volumes defined by

$$V(shell) = V_i - V_{i+1} \tag{10}$$

with the index i increasing with the extinction of the contour. If there is only one YSO in the contour, we assume an uncertainty of one YSO and plot only the point and an upper limit, corresponding to 1 ± 1 YSO. If there are no YSOs in the contour, we set the number to unity and plot the point and an upper limit based on 1 ± 1 YSOs. This approach allows us to show upper limits on log-log plots, following Heiderman et al. (2010).

The results for Class I sources are plotted in figure 1, along with the best fit relation and the predictions from equation 7 for an efficiency of 0.01. We do not include the upper limits (for zero or 1 YSO) in the fit, but they appear to be consistent. For reference, the conversion to number density (which includes all species) of particles is

$$n({\rm cm}^{-3}) = 17.2 \rho_{\rm gas}({\rm M}_\odot {\rm pc}^{-3}). \tag{11}$$

There is a strong correlation of ρ(SFR) and $\rho_{\rm gas}$, but it is steeper than predicted by the volumetric model. The best-fitting slope is 2.02 ± 0.07, more than 7 σ greater than the value of 1.5 predicted by the free-fall picture. A fit using robust estimation (minimizing the absolute deviation, without considering uncertainties), with the method of Press et al. (1992), yields a slope of 1.95. The prediction of equation 7 with $\epsilon_{\rm ff} = 0.01$ does get the mean value about right, but does not predict the trend.

However, the assumption of spherical symmetry for each shell could introduce errors and create an unrealistically steep correlation. Krumholz et al. (2012) also noted the observational difficulties of comparing volume densities, and they assumed that the volumetric law translated into a surface density relation of the same form. In particular, they predicted a linear relation between Σ(SFR) and $\Sigma_{\rm gas}/t_{\rm ff}$. This is easier to test as what we directly measure is surface density of gas via extinction and surface density of stars by counting in contours of extinction. We do have to use volume density to compute the free fall time. The result is shown in figure 2, once again with the theory plotted assuming $\epsilon_{\rm ff} = 0.01$. In this plot, the theory predicts the mean star formation rates fairly well, but the best fit slope is 1.47 ± 0.06, larger than the predicted slope of unity by 7 σ. Robust estimation yields 1.32.

Krumholz et al. (2012) actually used the properties of the whole cloud rather than within contours of extinction (their table 2). In this case, all YSOs, not just the Class I objects, can be used, because even Class II sources are unlikely to leave the entire cloud. The free-fall time is computed from the mean cloud density. We plot the same quantities as Krumholz et al. (2012), but using the latest YSO catalogs, in Fig. 3. As in Fig. 2, the theory predicts the mean Σ(SFR) reasonably correctly but in this case, there is no convincing correlation in the data (Pearson's $r = 0.35$; for this number of data points $r > 0.61$ is required for a statistically significant correlation). This is a bit puzzling because the points indicated by "MW clouds" in Fig. 3 of Krumholz et al. (2012) do appear to be correlated. This impression of a correlation arises because Krumholz et al. (2012) plotted the same clouds twice, but the second time with values taken from a contour with higher extinction values. Plotting the same clouds twice in Fig. 3 of Krumholz et al. (2012) effectively mixes our Fig. 1, which shows a very steep correlation *within* clouds, and Fig. 3, which shows no convincing correlation from one cloud to another. Lada et al. (2013) have also emphasized that there is a Schmidt relation (equation 1) *within* clouds but not *between* clouds.

3.3. *Tests of a Crossing Time Model*

We have also tested the crossing time instead of $t_{\rm ff}$ as the relevant timescale. We define $t_{\rm cross}$ as the time for a disturbance traveling at the turbulent equivalent of the mean speed to cross the entire cloud (twice the size, which is defined as the equivalent of the radius). The turbulent speed was calculated from the linewidth measured for the cloud, preferably an average over the cloud in the ^{13}CO $J = 1 \rightarrow 0$ line, but occasionally resorting to other tracers (see the Appendix for the sources of velocity data). The mean speed, related to the FWHM linewidth by a factor of 0.678, was used for the calculation. The plot of log Σ(SFR) versus log($\Sigma_{\rm gas}/t_{\rm cross}$) (Fig. 4) shows no correlation at all, with Pearson's $r = 0.22$. Crossing times may be relevant on larger or smaller scales, but we find no evidence that they matter on the scales of the nearby clouds.

3.4. *Tests of Threshold Idea*

For the clouds as a whole, Lada et al. (2010) have already provided the evidence for a better correlation between star formation and cloud mass if the cloud mass is restricted to the mass above a threshold surface density. Here we look at the data in other ways.

We divide each cloud into two regions separated by the contour of $A_V = 8$. Both Lada et al. (2010) and Heiderman et al. (2010) have suggested a threshold near this value of extinction. For $A_V < 8$, we will use the term

"low" and for $A_V \geq 8$, we will use the term "high." For comparison to large-scale studies, we aggregate all the YSOs and mass into the sum over each region. We do the same for Class I sources alone. We then compute a single value for the surface density of the star formation rate by dividing the total, based on the total number of YSOs, a mean mass of 0.5 $M_\odot$, and a duration of the infrared excess of 2 Myr (0.55 Myr for the Class I sources), and assign uncertainties in these mean values, based on counting statistics. We calculate the mean surface density as the total mass divided by the total surface area and assign an uncertainty as the range of mean surface densities for both low and high surface density regions.

The results (Fig. 5) are quite striking. The mean surface density of YSOs in the high region is 6.7 times the mean in the low region. For Class I sources, the ratio is 14. These results are consistent with the proposal of a threshold at $A_V \sim 8$ mag. In terms of raw numbers, of the 2915 YSOs in the new catalogs, 64% are projected onto high extinction parts of the cloud. Since some of the older YSOs could have left their birthplaces, this is a lower limit. If we restrict attention to Class I sources, the fraction rises to 77%. The cumulative area of all the clouds above this surface density is only 20% of that in all the clouds above $A_V = 2$, and the cumulative mass is only 38% of the total above $A_V = 2$. The result is further diluted by the fact that two large clouds were not mapped by Spitzer down to $A_V = 2$, so the total area and mass below $A_V = 8$ is undercounted. Finally, there is probably at least a factor of two more mass below $A_V = 2$ in CO-emitting gas (Goldsmith et al. 2008). In summary, the great majority of star formation occurs in a small fraction of the cloud area or mass.

The most direct test of the Lada et al. (2012) proposal (equation 8 or 9) is to plot the star formation rate versus the mass of dense gas. However, a plot of SFR versus gas mass naturally shows a correlation because big clouds tend to produce more stars. Instead we first plot the "efficiency" in the sense of SFR in the dense gas over the mass of dense gas ($\dot{M}_*/\ M_{\rm dense}$) versus the mass of dense gas (plotting logarithms) and look at the scatter (Fig. 6). We used the total number of YSOs within the $A_V = 8$ mag contour to measure the SFR and the mass inside that contour to measure the mass of dense gas. The mean and standard deviation of $\log(\dot{M}_*/M_{\rm dense})$ is -1.61 ± 0.23. The dispersion is comparable to the observational uncertainties and the likely systematic uncertainties (about 0.3 in the log). In contrast, if we plot the same quantities for the total SFR in the whole cloud and the total mass of the cloud, we obtain $\langle \log \dot{M}_*/M_{\rm cloud} \rangle = -2.06 \pm 0.83$, resulting in a standard deviation that is 3.6 times larger and substantially larger than both observational and likely systematic uncertainties (Fig. 7). The dense gas clearly yields a much more accurate prediction of the SFR. No obvious trend in the efficiency is seen in either figure 6 or 7 over more than two orders of magnitude in the corresponding gas mass, consistent with a roughly linear proportionality. Versions of these figures with data from additional clouds studied by Lada et al. (2010) added are shown in Padoan et al. (2013). While further assumptions are needed to add those clouds, they are consistent with the clouds shown here.

Having shown that the dispersion of star formation rate over dense gas mass is quite low, we now plot directly the star formation rate versus the mass of dense gas (equation 9). The results (black points) are plotted in Figure 8. The points show a strong correlation and lie reasonably close to the line representing equation 9. Fitting the data, we obtain $\dot{M}_*(\mathrm{M}_\odot\ \mathrm{Myr}^{-1}) = 0.041 {M_{\rm dense}}^{0.89}$ with a correlation coefficient of 0.963. The coeficient is 0.9 times that found by Lada et al. (2012), using a somewhat different set of clouds and threshold.

Lada et al. (2012) pointed out that their equation has a coefficient about 3.8 times that found by Wu et al. (2005). Vutisalchavakul & Evans (2013) have reexamined some of the massive dense clumps studied by Wu et al. (2005) to get better SFR by using radio continuum and integrating over the whole H II region. We plot these SFRs in red using the mass from the maps of HCN $J = 1 \rightarrow 0$ from Wu et al. (2010), where both measurements exist. These are broadly consistent with the prediction now, but there is a caveat. Massive stars destroy their environment rapidly, so the H II region is substantially larger than the remaining dense clump. Thus the original mass of dense gas was probably larger, which would move the massive dense clumps to the right in the figure. If we ignore that issue and fit the combination of the nearby clouds and the massive clumps, the result is $\dot{M}_*(\mathrm{M}_\odot\ \mathrm{Myr}^{-1}) = 0.040 {M_{\rm dense}}^{0.90}$ with a correlation coefficient of 0.924. The normalizing coefficient is close to that of Lada et al. (2012).

4. DISCUSSION

The tests presented above do not favor a picture in which the free fall time, computed from the mean density of a cloud, is an important factor in predicting the star formation rate within the cloud. This result is not surprising because clouds do not appear to be collapsing at free fall (e.g., Zuckerman & Evans 1974). When the free-fall time is computed more locally, in nested contours, and a low efficiency factor per free-fall time is included, models that predict $\rho(\mathrm{SFR}) \propto {\rho_{\rm gas}}^{1.5}$ get the magnitude of ρ(SFR) roughly right, but the actual ρ(SFR) increases more rapidly ($\rho(\mathrm{SFR}) \propto {\rho_{\rm gas}}^{2}$). The free-fall time may become relevant, if ever, only on scales of individual infalling envelopes. The cloud crossing time also does not seem to be very useful as a predictor of star formation rates, though crossing times may be relevant on larger or smaller scales.

The threshold model is really just a codification of observational facts. Star formation is observed to be highly concentrated in regions of high surface density, more concentrated than can be explained with models using a free-fall time calculated from a mean density. It is important to clarify what Lada et al. (2012) meant by a threshold. They say "Furthermore, our data are consistent with the existence of a column density threshold for star formation activity above which the SFR appears to be linearly correlated with the total cloud mass above the threshold." They did not claim that there was **no** star formation below the threshold. Similarly Heiderman et al. (2010) said "A steep increase and possible leveling off in Σ(SFR) at a threshold $\Sigma_{thresh} \sim$ 100 to 200 $\mathrm{M}_\odot\ \mathrm{pc}^{-2}$ is seen..." One might interpret these statements as advocating a step function or a "precise" boundary between star-forming

and non-star-forming gas. That was not the intent of either set of authors.

Indeed, Lada et al. (2013) have tested models with a step function (Heaviside function) in 4 clouds, finding that two are consistent with such an extreme definition of threshold, while two are not. They conclude that a Heaviside function, while possible in some clouds, is too extreme for a general definition of threshold.

A second point that needs clarification is the scale over which the gas surface density is measured. One could argue that a surface density threshold is a tautology because stars can only form in dense gas. The scale over which the surface density is measured in the nearby clouds is limited by the resolution of the extinction maps to 270″, which corresponds to 0.34 pc at the mean distance. The mean area of the $A_V = 8$ contour corresponds to a radius of 2.5 pc. The gas density measured from extinction corresponds to scales of clumps which may contain many individual dense cores, the sites of individual star formation. There is no a priori reason why such dense cores cannot form in regions of lower average surface density, in which case they could be spread more evenly over the cloud. Some occasionally do form in regions of lower extinction, but they are rare. To be specific, Enoch et al. (2008) found that 75% of prestellar cores were found above $A_V = 6.5$, 8, and 19.5 mag in Perseus, Serpens, and Ophiuchus, respectively. No cores were found below $A_V = 7$ or 15 mag in Serpens and Ophiuchus, respectively. The constraints on cores hosting protostars were even tighter.

The issue of scale is also relevant to the interpretation of the continued rise of star formation rate surface density roughly proportional to the square of gas surface density, even above the threshold of $A_V = 8$ mag, in young clusters (Gutermuth et al. 2011). Our data do not disagree with this result, but we consider it to be probing the distribution of star formation *within* a clump rather than constraining the definition of a star forming clump, defined on larger scales to include the bulk of star formation.

One might also question whether the star formation rates in these clouds are low because they are young, and star formation accelerates. While observers lack the ability to determine cloud ages, we can make a crude measure by examining the class distribution of the YSOs. For the clouds as a whole, we computed an "age indicator" from the relative number of sources in older and younger classes as follows:

$$Age = [N(YSOs) - N(I) - N(F)]/N(YSOs) \quad (12)$$

where $N(YSOs)$ is total number of YSOs, $N(I)$ is the number of Class I objects, and $N(F)$ is the number of Flat spectrum sources. All but 4 clouds have "age" greater than 0.5, indicating a preponderance of Class II and Class III objects, and hence that star formation has been proceeding for at least 1-2 Myr. Three of the four exceptions are small clouds with only one or two YSOs; the fourth, with "age" of 0.5, is IC5146 NW, with 38 YSOs. For clouds with a sufficient number of YSOs to determine the "age", there is no obvious evidence for acceleration, but the dynamic range is too small to provide a strong test.

While a complete survey of theoretical ideas is beyond the scope of this paper, a few can be mentioned that address the observations discussed here. Burkert & Hartmann (2013) have argued that a model of formation of molecular clouds from galactic hydrodynamical flows and subsequent gravitation collapse, while dense gas continues to form during star formation, can match the observations presented by Heiderman et al. (2010). Federrath & Klessen (2012) show that models and simulations with MHD turbulence and local free-fall times also match the data, with certain assumptions. Our results suggest that the free-fall time calculated from large-scale mean densities is not a useful parameter for predicting star formation rates, but $t_{\rm ff}$ calculated more locally may be relevant, as suggested by Hennebelle & Chabrier (2011). Federrath & Klessen (2012) also focus on the remaining scatter in the Heiderman et al. (2010) data, which is indeed substantial. They suggest that virial parameter, Mach number, the nature of turbulent forcing, and magnetic field all contribute to this scatter. At this point, our knowledge of these parameters for these clouds does now allow sharper tests of that picture. In particular, the small variation in linewidth among this sample (Table 1) provides too small a lever arm. However, we can say that testing the dependence on these parameters will be better done after the first order dependence on cloud, or better dense gas, mass has been removed.

Theorists modeling gravoturbulent fragmentation generally argue that volume density, rather than column density, should be the controlling factor (see Padoan et al. 2013 for a review), and many theories invoke a critical volume density for star formation. Lada et al. (2012) suggest a volume density of $n \sim 10^4$ cm^{-3} as the value that corresponds to the surface density threshold. The average volume density in the regions above the $A_V = 8$ mag threshold in this sample is $\langle n \rangle = (6.1 \pm 4.4) \times 10^3$ cm^{-3}, roughly consistent, but lower than 10^4 cm^{-3} and with a rather large dispersion. At this point, column density, rather than volume density, looks more likely to be the controlling factor. As discussed in more detail by Heiderman et al. (2010), models in which magnetic fields (Mouschovias & Spitzer 1976) or photoionization (McKee 1989) regulate star formation, while out of theoretical fashion, are still the models most consistent with the actual observations. A more recent treatment also shows the relevance of column density via self-shielding, and offers a suggested explanation of the threshold value around $A_V = 8$ mag (Clark & Glover 2013).

While the structures bearing prestellar or protostellar cores often appeared filamentary in the extinction maps, the resolution was insufficient to delinate the structure well. More recent mapping with Herschel shows that prestellar and protostellar cores are closely confined to narrow filaments with surface density corresponding to $A_V = 10$ mag (André et al. 2010) and average width (FWHM) of 0.10 ± 0.03 pc (Arzoumanian et al. 2011). In contrast, filaments with $A_V \sim 2$ mag and similar or smaller width contained no star formation (André et al. 2010). Further study of these filaments is likely to lead to a deeper understanding of the threshold picture (e.g., Arzoumanian et al. 2013). Testing for a threshold in mass per unit length along a filament will be necessary.

5. CONCLUSIONS

While a star formation relation employing a mean $t_{\rm ff}$ seems to work on very large scales of galaxies (Krumholz et al. 2012) and to predict roughly the mean rate of star formation in nearby clouds, with $\epsilon_{\rm ff} = 0.01$ (Krumholz & McKee 2005), it does not predict the behavior of star formation rates on small scales within molecular clouds. These observed rates show a steeper dependence on the surface density or volume density per free-fall time than predicted. When applied to whole clouds, the data show no significant correlation with $\Sigma_{\rm gas}/t_{\rm ff}$, with $t_{\rm ff}$ calculated from the mean cloud density, as advocated by Krumholz et al. (2012). If the crossing time is substituted for the free fall time, no correlation at all is seen.

In contrast, the picture in which the star formation rate is linearly proportional to the mass of dense gas above a threshold surface density (Lada et al. 2012), corresponding to $A_V = 8$ mag, matches the data for nearby clouds with very low dispersion. Using new determinations of the star formation rate in massive dense clumps (Vutisalchavakul & Evans 2013), those data are matched reasonably well also by the same relation (equation 9), but there are more uncertainies in those distant clumps, where counting of YSOs is not practical. Since this same relation works well for galaxies, using the HCN emission to estimate crudely the mass of dense gas, it would appear to be the best relation to use in simulations of sufficient resolution to locate the dense gas. However, the particular threshold that applies to nearby clouds may not apply in other regions, especially those with lower metallicity or much stronger radiation fields (cf. clouds in the CMZ, Longmore et al. 2013). In any case, removing the first order dependence on the mass of dense gas is necessary before testing the importance of other factors suggested by theorists.

We thank L. Hartmann, P. Padoan, and C. Federrath for helpful discussions and M. Dunham for compiling the YSO lists for the Gould Belt project. This research was supported by NSF Grant AST-1109116 to the University of Texas at Austin. NJE thanks the European Southern Observatory, Santiago, for hospitality during an extended visit when this work was begun.

APPENDIX

APPENDIX A: INFORMATION ON CLOUDS

The two pieces of information about the clouds from outside the c2d or Gould Belt data are the distances and velocity dispersions. The distances are taken from Dunham et al. (2013), who give references, but we also give separate distances to the five clouds in Cepheus, based on Kirk et al. (2009).

The velocities in Table 1 are the full width at half maximum of the ^{13}CO $J = 1 \rightarrow 0$ line, whenever possible. Ideally, these are based on an average over the whole cloud, but in many cases, only the linewidths for individual points are available. In that case, the values in the table are averaged by hand. In some cases, the linewidths are at best educated guesses, based on other isotopologues or species. Brief discussions of each cloud with references are given below.

Aquila

This region lies in the "Serpens-Aquila rift" and has been called "Serpens South", "Serpens-Aquila", and "Aquila." We adopt the last convention. Gutermuth et al. (2008) describe the Spitzer data, and Maury et al. (2011) present millimeter continuum data. The distance is taken from Maury et al. (2011), which places it closer to us than the Serpens cloud, formerly considered to be at the same distance. No data on ^{13}CO $J = 1 \rightarrow 0$ were found, so a linewidth of 3.0 km s^{-1} was estimated from line profiles of HCO$^+$ $J = 4 \rightarrow 3$ found in Nakamura et al. (2011). This estimate is clearly quite uncertain.

Auriga

This region was identified as a single entity composed of a number of Lynds dark clouds by Lada et al. (2009). It has also been called the "California Cloud", or the "California-Auriga" cloud (Harvey et al. 2013). Some information on ^{13}CO found for this cloud refers to NGC5179, the nebula around Lk Hα 101, where Δv(^{13}CO) was measured to be about 2 km s^{-1} based on two spectra in Knapp et al. (1976). These may not be representative of the rest of the cloud. A different part of the cloud was mapped in ^{13}CO by Herbertz et al. (1991), including the region around L1442, L1449, and L1456. Based on averaging their Gaussian standard deviations and multiplying by 2.35 to get FWHM, values of Δv = 1.41 to 1.69 km s^{-1} were obtained for parts of the cloud. We adopt 1.7 km s^{-1}, based on these fragmentary measurements, but we emphasize the uncertainty.

Cepheus clouds

For the Cepheus flare, Kirk et al. (2009) has published analysis of the six separate regions, including separate distance and velocity measurements. The clouds are labeled by Lynds numbers. We have made the following associations with our Spitzer regions: Ceph-1 corresponds to L1251+L1247 with a linewidth of ^{13}CO of 1.9 km s^{-1}; Ceph-2 corresponds to L1241 with Δv(^{13}CO) of 2.2 km s^{-1}; Ceph-3 corresponds to L1172+L1144 with Δv(^{13}CO) of 1.6 km s^{-1}; Ceph-4 corresponds to L1148+L1152+L1155 with Δv(^{13}CO) of 1.0 km s^{-1}; Ceph-5 corresponds to L1228 with Δv(^{13}CO) of 1.6 km s^{-1}.

Chamaeleon

Vilas-Boas et al. (1994) give mean Δv(^{13}CO) for Cha II and III, but not for Cha I. Cha I was mapped by Mizuno et al. (1998) in ^{13}CO, but no information on linewidth was given. It was also mapped in CO by Mizuno et al. (2001), who give a Δv for CO of 2.0 km s^{-1}. They also give 2.8 km s^{-1} and 2.6 km s^{-1} for Cha II and III respectively. Based on ratios of the ^{13}CO to CO line widths in those clouds of 0.426, we used $0.426 \times 2.0 = 0.85$ km s^{-1} for ^{13}CO in Cha I.

Corona Australis

The cloud has been studied in considerable detail, but we had to go back to Loren (1979) to get data on ^{13}CO. From a map of Δv of ^{13}CO $J = 1 \rightarrow 0$ over the cloud, one can see values from 1.0 to 2.0 km s^{-1}, with 1.5 km s^{-1} being the most characteristic value.

IC5146

The velocities are from Dobashi et al. (1992). For IC5146 E, we use cloud E, which has $\Delta v = 2.45 \pm 0.3$; for IC5146 NW, we use cloud C, which has $\Delta v = 2.04 \pm 0.42$, where these are the average and standard deviation of all relevant Δv(^{13}CO) in their Table 1.

Lupus

Hara et al. (1999) mapped the area in ^{13}CO $J = 1 \rightarrow 0$, obtaining typical Δv of 1.2 km s^{-1}, but there is considerable variation in the region. We now adopt values for each cloud separately. We use Hara et al. (1999) for Lupus V and VI. For Lupus I, III, and IV, the linewidths come from ^{13}CO $J = 2 \rightarrow 1$ maps by Tothill et al. (2009), but averaging the mean and median linewidths (N. Tothill, private communication) as was also done for Ophiuchus, Perseus, and Serpens (below).

Musca

Vilas-Boas et al. (1994) gives Δv(^{13}CO) of 0.8 km s^{-1} for Musca.

Ophiuchus

The linewidth information was given in Evans et al. (2009), originally provided by J. Pineda (2008, private communiction) using the COMPLETE maps (Ridge et al. 2006). The values represent the average of the mean and median linewidths averaged over the clouds.

Ophiuchus North

This region was identified as Scorpius in the Gould Belt nomenclature, but it is now known as Ophiuchus-North, since it is not actually in Scorpius. Hatchell et al. (2012) published the Gould Belt data under this name. This region was mapped by Nozawa et al. (1991) in ^{13}CO, and the identification of cores in the notation of Nozawa et al. (1991) with the Spitzer regions was made using the table in Hatchell et al. (2012).

Perseus

The linewidth information was obtained in the same way as for Ophiuchus.

Serpens

The linewidth information was obtained in the same way as for Ophiuchus. The distance is updated from Heiderman et al. (2010) based on the VLBA parallax of the Herbig Ae/Be star, EC95, yielding a distance of 429 ± 2 pc (Dzib et al. 2011).

APPENDIX B: ERROR PROPAGATION

The uncertainties plotted on each point in a plot are based on observational uncertainties only. In some plots, a separate uncertainty is plotted to indicate the estimated systematic uncertainties for the sample as a whole. The basic observational quantities are the number counts of YSOs, the extinction, and the distance. The uncertainty in the extinction propagates immediately into the mass surface density of gas, while the distance uncertainty propagates into the uncertainty in the area, through the conversion of angles to linear area. The further propagation of observational uncertainty in those quantities into the derived quantities is explained next, followed by a discussion of systematic uncertainties.

For the star formation rate, the uncertainties are based on counting statistics:

$$\sigma(\dot{M}_*) = (\sqrt{N}/N)\dot{M}_* \tag{B1}$$

where N is the number of YSOs in that sample (Class I for Figs. 1 and 2 and the upper panel of Fig. 5; all classes for the other figures).

For Σ(SFR) $= \dot{M}_*/A$, where A is the area, the uncertainties include the uncertainty in the distance via the area:

$$\sigma(\Sigma(\mathrm{SFR})) = \Sigma(\mathrm{SFR}) \left[\left(\sigma(\dot{M}_*)/\dot{M}_* \right)^2 + (\sigma(A)/A)^2 \right]^{0.5} \tag{B2}$$

For ρ(SFR) (Fig. 1), we express it as

$$\rho(\mathrm{SFR}) = \dot{M}_*/V = \frac{\dot{M}_*}{0.752 A^{1.5}} \tag{B3}$$

where V is the volume. Then

$$\sigma(\rho(\mathrm{SFR})) = \rho(\mathrm{SFR}) \left[\left(\frac{\sigma(\dot{M}_*)}{\dot{M}_*} \right)^2 + \left(\frac{1.5\sigma(A)}{A} \right)^2 \right]^{0.5} \tag{B4}$$

For masses ($M_{\rm cloud}$ or $M_{\rm dense}$), the uncertainties include the uncertainty in the extinction from the extinction maps and the distance uncertainty through the uncertainty in the area since mass is measured from extinction times area. Observational uncertainties were not available for the massive dense cores plotted in figure 8, so we assumed uncertainties of 0.30 in $\log(\dot{M}_*)$ and 0.15 in $\log(M_{\rm dense})$.

For surface densities of gas, the distance uncertainty does not enter because both mass and area scale as d^2, so the uncertainty is just the uncertainty in the extinction maps.

For volume densities of gas (Fig. 1), the distance uncertainties do enter. We express the gas density as

$$\rho_{\rm gas} = M/V = \frac{\Sigma_{\rm gas}}{0.752 A^{0.5}} \tag{B5}$$

In this form,

$$\sigma(\rho_{\rm gas}) = \rho_{\rm gas} \left[\left(\frac{\sigma(\Sigma_{\rm gas})}{\Sigma_{\rm gas}} \right)^2 + \left(\frac{0.5\sigma(A)}{A} \right)^2 \right]^{0.5} \tag{B6}$$

For figure 3, where we plot $\Sigma_{\rm gas}/t_{\rm ff}$, we can write

$$\Sigma_{\rm gas}/t_{\rm ff} = \frac{\Sigma_{\rm gas} \rho_{\rm gas}^{0.5}}{8.08} = 0.143 {\Sigma_{\rm gas}}^{1.5} A^{-0.25} \tag{B7}$$

using

$$\rho_{\rm gas} = \frac{M_{\rm gas}}{0.752 A^{1.5}} = \frac{\Sigma_{\rm gas}}{0.752 A^{0.5}} \tag{B8}$$

Then

$$\sigma(\Sigma_{\rm gas}/t_{\rm ff}) = \frac{\Sigma_{\rm gas}}{t_{\rm ff}} \left[\left(\frac{1.5\sigma(\Sigma_{\rm gas})}{\Sigma_{\rm gas}} \right)^2 + \left(\frac{0.25\sigma(A)}{A} \right)^2 \right]^{0.5} \tag{B9}$$

so, the distance uncertainty enters weakly, only through the area.

For figure 4, the distance enters via the size, which depends on the square root of the area. Using the facts that the mean speed is 0.678Δv and that 1 km s^{-1} is 1.023 pc Myr^{-1}, we can write

$$\Sigma_{\rm gas}/t_{\rm cross} = \frac{\Sigma_{\rm gas} \langle v \rangle}{2r} = 0.6165 \frac{\Sigma_{\rm gas} \Delta \mathrm{v}(\mathrm{km\ s^{-1}})}{A^{0.5}} \tag{B10}$$

and

$$\sigma(\Sigma_{\rm gas}/t_{\rm cross}) = \frac{\Sigma_{\rm gas}}{t_{\rm cross}} \times \left[\left(\frac{\sigma(\Sigma_{\rm gas})}{\Sigma_{\rm gas}} \right)^2 + \left(\frac{0.5\sigma(A)}{A} \right)^2 + \left(\frac{\sigma(\Delta \mathrm{v})}{\Delta \mathrm{v}} \right)^2 \right]^{0.5}. \tag{B11}$$

The dominant source of uncertainty is the Δv, and most lack reliable uncertainties. We have taken an uncertainty of 30% for each cloud in $\sigma(\Delta \mathrm{v})$.

The uncertainties in quantities were propagated to asymmetric uncertainties in the logarithms for the plots by taking the logarithms of the minimum and maximum values of the quantity. Because the fitting routine could use only symmetric uncertainties, we used the maximum of the two asymmetric errors for the fit.

In addition to the observational uncertainties, there are systematic uncertainties that affect all points in the same way. These are not included in the error bars on each point because they do not affect the issue of correlations or slopes. They would affect scaling of the axes, offsets for fits, and the absolute value of the mean values in figures 6 and 7.

The star formation rate is computed from the counts of YSOs, a mean mass per star, and a timescale over which those YSOs are visible (Evans et al. 2009). As noted earlier, the counts of YSOs could be low by about 30% if less cautious methods of removing contaminants are adopted. The counts of Class I objects could decrease by about 50% if many sources classified as Class I are found not to be associated with dense gas, but in that case the timescale would be decreased by the same factor, leaving the rate unchanged. The mean stellar mass is taken to be 0.5 $M_\odot$, and the half-life for YSOs, as identified by the c2d and Gould Belt programs, was taken to be 2 Myr. The half-lives

Table 1
Basic Data on Clouds[1]

Cloud -	Dist. (pc)	Size (pc)	$\dot{M}_*$ ($M_\odot$ Myr^{-1})	M_{cloud} ($M_\odot$)	M_{dense} ($M_\odot$)	Σ(SFR) ($M_\odot$ Myr^{-1} pc^{-2})	Σ_{gas} ($M_\odot$ pc^{-2})	t_{ff} (Myr)	Δv (km s^{-1})	t_{cross} (Myr)
Aquila	260	7.56	322.3	24446	16034	1.80	136.2	2.20	3.00	7.26
Auriga N	450	1.31	0.50	503	13	0.09	92.78	1.11	1.70	2.22
Auriga	450	5.98	36.0	10391	1134	0.32	92.37	2.38	1.70	10.1
Cepheus 1	300	1.75	8.50	671	5.5	0.89	69.91	1.48	1.90	2.65
Cepheus 2	300	1.46	0.00	499	12	0.00	74.18	1.31	2.20	1.92
Cepheus 3	288	1.75	10.5	633	41	1.09	65.49	1.53	1.60	3.16
Cepheus 4	325	1.08	0.50	267	0	0.14	73.31	1.13	1.00	3.11
Cepheus 5	200	1.07	4.75	233	31	1.33	65.32	1.19	1.60	1.92
Cha I	150	1.30	20.5	482	176	3.88	91.18	1.11	0.85	4.40
Cha II	178	1.78	6.00	637	64	0.61	64.34	1.55	1.20	4.26
Cha III	150	2.24	1.00	746	0	0.06	47.37	2.03	1.10	5.86
Corona Aus.	130	0.98	10.5	279	139	3.47	92.16	0.96	1.50	1.89
IC5146 E	950	4.42	23.25	3365	0	0.38	54.79	2.65	2.45	5.20
IC5146 NW	950	5.28	9.50	5179	92	0.11	59.13	2.79	2.04	7.46
Lupus I	150	1.68	3.25	512	39	0.37	57.86	1.59	2.17	2.23
Lupus III	200	2.22	17.0	912	96	1.10	59.08	1.81	2.11	3.03
Lupus IV	150	0.90	3.00	189	50	1.19	75.14	1.02	1.53	1.69
Lupus V	150	1.93	10.5	704	0	0.90	60.50	1.66	1.20	4.62
Lupus VI	150	1.46	11.0	454	4.3	1.63	67.50	1.37	1.20	3.52
Musca	160	1.47	3.00	335	0	0.44	49.15	1.62	0.80	5.31
Ophiuchus	125	3.08	72.75	3128	1209	2.44	104.8	1.60	0.94	9.45
Oph North 1	130	0.49	0.25	66	11	0.33	86.97	0.70	0.80	1.77
Oph North 2	130	0.46	0.00	68	26	0.00	102.7	0.63	1.37	0.97
Oph North 3	130	0.94	1.25	258	64	0.45	94.13	0.93	1.00	2.72
Oph North 4	130	0.58	0.00	76	0	0.00	71.83	0.84	1.23	1.37
Oph North 5	130	0.39	0.00	34	0	0.00	69.65	0.70	1.23	0.93
Oph North 6	130	0.70	0.75	116	12	0.48	74.85	0.90	0.85	2.38
Perseus	250	4.83	96.25	6586	2147	1.32	89.99	2.16	1.54	9.03
Serpens	429	3.92	56.0	6520	4213	1.16	135.1	1.59	2.16	5.23
Median	150	1.47	6.0	504	39	0.48	73.3	1.48	1.50	3.11
Mean	256	2.17	25.1	2355	885	0.89	78.6	1.47	1.52	3.99
Stdev	220	1.83	61.7	4940	3044	0.99	22.2	0.58	0.56	2.59

[1] These cloud values refer to extinction contours of $A_V = 2$ ($A_V = 6$ for Serpens and $A_V = 3$ for Ophiuchus)

of earlier stages are scaled to that value, and we used 0.55 Myr for Class I objects. The mean stellar mass is taken from IMF models. The uncertainties in these numbers are probably a factor of 2, which propagates directly into $\dot{M}_*$ and Σ(SFR).

For the masses of gas, the conversion of extinction to surface density or mass is the main systematic uncertainty. We use the Case A models of Weingartner and Draine for $R_V = 5.5$, as updated on the website noted in §1. These are consistent with our earlier paper (Heiderman et al. 2010), and more or less consistent with Lada et al. (2010). However, in a more recent paper, Lada et al. (2013) use a different model of dust, closer to Case B models. These match data well (Ascenso et al. 2013), but have some theoretical difficulties (Draine, personal communication). The Case B models imply a higher ratio of Σ_{gas}/A_V by a factor of 1.49. This is not a two sided error, but instead a possible increase in M_{cloud}, M_{dense}, and Σ_{gas}, all by the factor 1.49. The effect on Σ_{gas}/t_{ff} would be an increase by a factor of $1.49^{1.5} = 1.82$.

REFERENCES

André, P., Men'shchikov, A., Bontemps, S., et al. 2010, A&A, 518, L102
André, P., Men'shchikov, A., Koenyves, V., et al. 2011, in Stellar Clusters & Associations: A RIA Workshop on Gaia, 321–328
Arzoumanian, D., André, P., Didelon, P., et al. 2011, A&A, 529, L6
Arzoumanian, D., André, P., Peretto, N., & Könyves, V. 2013, A&A, 553, A119
Ascenso, J., Lada, C. J., Alves, J., Román-Zúñiga, C. G., & Lombardi, M. 2013, A&A, 549, A135
Bigiel, F., Leroy, A., Walter, F., et al. 2008, AJ, 136, 2846
Bolatto, A. D., Wolfire, M., & Leroy, A. K. 2013, ARA&A, 51, 207
Burkert, A. & Hartmann, L. 2013, ApJ, 773, 48
Chabrier, G. 2003, PASP, 115, 763
Chapman, N. L., Mundy, L. G., Lai, S.-P., & Evans, II, N. J. 2009, ApJ, 690, 496
Clark, P. C. & Glover, S. C. O. 2013, ArXiv e-prints
Daddi, E., Elbaz, D., Walter, F., et al. 2010, ApJ, 714, L118
Dobashi, K., Yonekura, Y., Mizuno, A., & Fukui, Y. 1992, AJ, 104, 1525
Dunham, M. M., Arce, H. G., Allen, L. E., et al. 2013, AJ, 145, 94
Dzib, S., Loinard, L., Mioduszewski, A. J., et al. 2011, in Revista Mexicana de Astronomia y Astrofisica Conference Series, Vol. 40, Revista Mexicana de Astronomia y Astrofisica Conference Series, 231–232
Elmegreen, B. G. 2000, ApJ, 530, 277

Enoch, M. L., Evans, II, N. J., Sargent, A. I., & Glenn, J. 2009, ApJ, 692, 973
Enoch, M. L., Evans, II, N. J., Sargent, A. I., et al. 2008, ApJ, 684, 1240
Enoch, M. L., Glenn, J., Evans, II, N. J., et al. 2007, ApJ, 666, 982
Evans, N. J., et. al.. 2007, Final Delivery of Data from the c2d Legacy Project: IRAC and MIPS (Pasadena: SSC), http://ssc.spitzer.caltech.edu/legacy/all.html
Evans, II, N. J., Allen, L. E., Blake, G. A., et al. 2003, PASP, 115, 965
Evans, II, N. J., Dunham, M. M., Jørgensen, J. K., et al. 2009, ApJS, 181, 321
Federrath, C. & Klessen, R. S. 2012, ApJ, 761, 156
Gao, Y. & Solomon, P. M. 2004, ApJ, 606, 271
Genzel, R., Tacconi, L. J., Gracia-Carpio, J., et al. 2010, MNRAS, 407, 2091
Goldsmith, P. F., Heyer, M., Narayanan, G., et al. 2008, ApJ, 680, 428
Gutermuth, R. A., Bourke, T. L., Allen, L. E., et al. 2008, ApJ, 673, L151
Gutermuth, R. A., Pipher, J. L., Megeath, S. T., et al. 2011, ApJ, 739, 84
Hara, A., Tachihara, K., Mizuno, A., et al. 1999, PASJ, 51, 895
Harvey, P., Merín, B., Huard, T. L., et al. 2007, ApJ, 663, 1149
Harvey, P. M., Fallscheer, C., Ginsburg, A., et al. 2013, ApJ, 764, 133
Hatchell, J., Terebey, S., Huard, T., et al. 2012, ApJ, 754, 104
Heiderman, A., Evans, II, N. J., Allen, L. E., Huard, T., & Heyer, M. 2010, ApJ, 723, 1019
Hennebelle, P. & Chabrier, G. 2011, ApJ, 743, L29
Herbertz, R., Ungerechts, H., & Winnewisser, G. 1991, A&A, 249, 483
Hsieh, T.-H. & Lai, S.-P. 2013, ApJS, 205, 5
Johnstone, D., Di Francesco, J., & Kirk, H. 2004, ApJ, 611, L45
Kennicutt, R. C. & Evans, N. J. 2012, ARA&A, 50, 531
Kennicutt, Jr., R. C. 1998, ApJ, 498, 541
Kirk, J. M., Ward-Thompson, D., Di Francesco, J., et al. 2009, ApJS, 185, 198
Knapp, G. R., Kuiper, T. B. H., Knapp, S. L., & Brown, R. L. 1976, ApJ, 206, 443
Kroupa, P. 2002, Science, 295, 82
Kruijssen, J. M. D., Longmore, S. N., Elmegreen, B. G., et al. 2013, ArXiv e-prints
Krumholz, M. R., Dekel, A., & McKee, C. F. 2012, ApJ, 745, 69
Krumholz, M. R. & McKee, C. F. 2005, ApJ, 630, 250
Krumholz, M. R. & Thompson, T. A. 2007, ApJ, 669, 289
Lada, C. J., Forbrich, J., Lombardi, M., & Alves, J. F. 2012, ApJ, 745, 190
Lada, C. J., Lombardi, M., & Alves, J. F. 2009, ApJ, 703, 52
Lada, C. J., Lombardi, M., & Alves, J. F. 2010, ApJ, 724, 687
Lada, C. J., Lombardi, M., Roman-Zuniga, C., Forbrich, J., & Alves, J. F. 2013, ApJ, 778, 133
Lada, E. A. 1992, ApJ, 393, L25
Leroy, A. K., Walter, F., Brinks, E., et al. 2008, AJ, 136, 2782
Leroy, A. K., Walter, F., Sandstrom, K., et al. 2013, AJ, 146, 19
Li, W., Evans, II, N. J., & Lada, E. A. 1997, ApJ, 488, 277
Longmore, S. N., Bally, J., Testi, L., et al. 2013, MNRAS, 429, 987
Loren, R. B. 1979, ApJ, 227, 832
Maury, A. J., André, P., Men'shchikov, A., Könyves, V., & Bontemps, S. 2011, A&A, 535, A77
McKee, C. F. 1989, ApJ, 345, 782
Mizuno, A., Hayakawa, T., Yamaguchi, N., et al. 1998, ApJ, 507, L83
Mizuno, A., Yamaguchi, R., Tachihara, K., et al. 2001, PASJ, 53, 1071
Mouschovias, T. C. & Spitzer, Jr., L. 1976, ApJ, 210, 326
Nakamura, F., Sugitani, K., Shimajiri, Y., et al. 2011, ApJ, 737, 56
Narayanan, D., Cox, T. J., Shirley, Y., et al. 2008, ApJ, 684, 996
Ninkovic, S. & Trajkovska, V. 2006, Serbian Astronomical Journal, 172, 17
Nozawa, S., Mizuno, A., Teshima, Y., Ogawa, H., & Fukui, Y. 1991, ApJS, 77, 647
Oliveira, I., Merín, B., Pontoppidan, K. M., et al. 2009, ApJ, 691, 672
Onishi, T., Mizuno, A., Kawamura, A., Ogawa, H., & Fukui, Y. 1998, ApJ, 502, 296
Padoan, P., Federrath, C., Chabrier, G., et al. 2013, ArXiv e-prints
Press, W. H., Teukolsky, S. A., Vetterling, W. T., & Flannery, B. P. 1992, Numerical recipes in FORTRAN. The art of scientific computing
Ridge, N. A., Di Francesco, J., Kirk, H., et al. 2006, AJ, 131, 2921
Schmidt, M. 1959, ApJ, 129, 243
Schmidt, M. 1963, ApJ, 137, 758
Schruba, A., Leroy, A. K., Walter, F., et al. 2011, AJ, 142, 37
Snell, R. L., Carpenter, J. M., & Heyer, M. H. 2002, ApJ, 578, 229
Solomon, P. M. & Sage, L. J. 1988, ApJ, 334, 613
Spezzi, L., Alcalá, J. M., Covino, E., et al. 2008, ApJ, 680, 1295
Tothill, N. F. H., Löhr, A., Parshley, S. C., et al. 2009, ApJS, 185, 98
van Kempen, T. A., van Dishoeck, E. F., Salter, D. M., et al. 2009, A&A, 498, 167
Vilas-Boas, J. W. S., Myers, P. C., & Fuller, G. A. 1994, ApJ, 433, 96
Vutisalchavakul, N. & Evans, II, N. J. 2013, ApJ, 765, 129
Weingartner, J. C. & Draine, B. T. 2001, ApJ, 548, 296
Wu, J., Evans, II, N. J., Gao, Y., et al. 2005, ApJ, 635, L173
Wu, J., Evans, II, N. J., Shirley, Y. L., & Knez, C. 2010, ApJS, 188, 313
Zuckerman, B. & Evans, II, N. J. 1974, ApJ, 192, L149

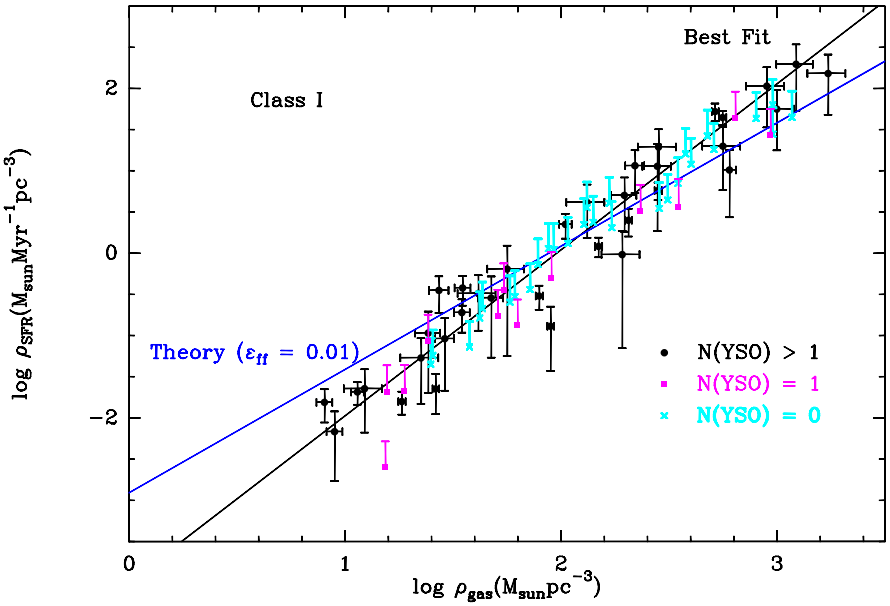

Figure 1. Plot of log(ρ(SFR)) versus log($\rho_{\rm gas}$) for Class I sources in the nearby clouds. The uncertainties are propagated into both axes for contours with more than one YSO. For contours with only 1 YSO, only upper limits are plotted since the uncertainties exceed the value. Likewise, contours with no YSOs are plotted as if they had one YSO, again with only upward uncertainties, assuming an uncertainty of 1 in the number of YSOs. The blue line is the prediction of equation 7. The black line is the result of a least-squares fit to the data.

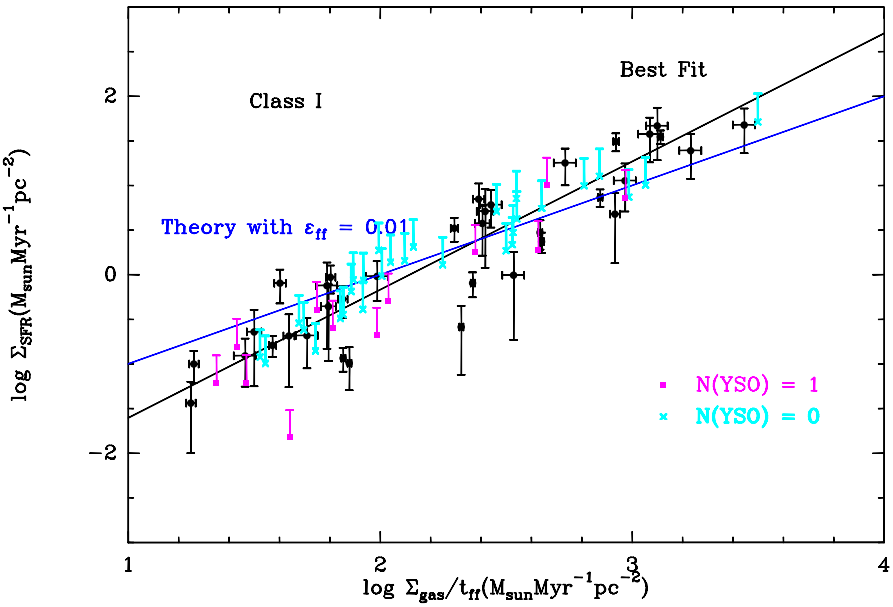

Figure 2. Plot of log(Σ(SFR)) versus log($\Sigma_{\rm gas}/t_{\rm ff}$) for Class I sources in the nearby clouds. The uncertainties are propagated into both axes for contours where the value exceeds the uncertainty. Only the points and the upper limits are plotted when the uncertainties exceed the value, but the data are consistent with negative infinity in the log. Likewise, contours with no YSOs are plotted as if they had one YSO, again with only upward uncertainties, assuming an uncertainty of 1 in the number of YSOs. The blue line is the prediction of equation 7, translated to surface densities. The black line is the result of a least-squares fit to the data.

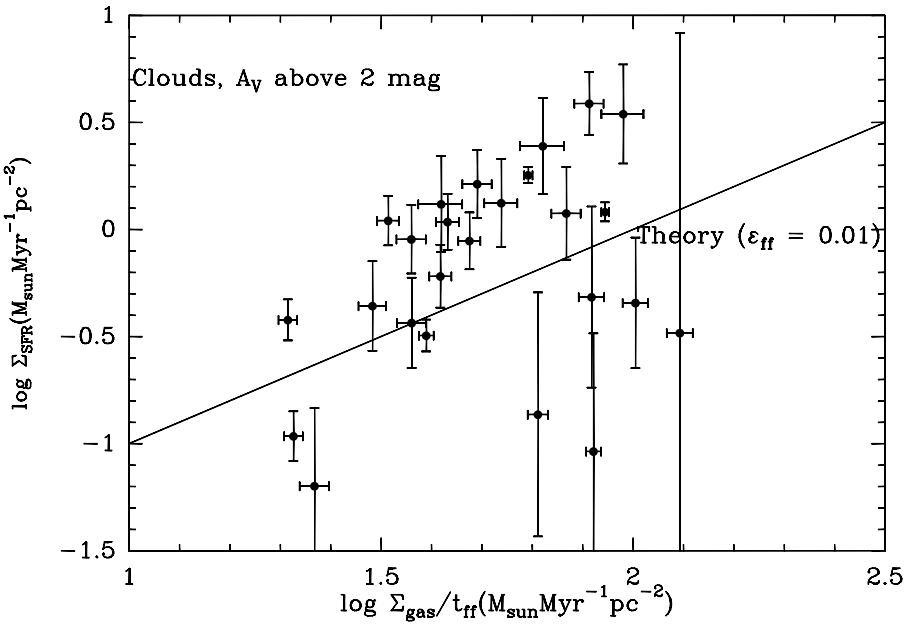

Figure 3. Plot of $\log(\Sigma(\mathrm{SFR}))$ versus $\log(\Sigma_{\mathrm{gas}}/t_{\mathrm{ff}})$ for all YSOs in the nearby clouds, on a cloud by cloud basis. Only clouds with at least one YSO are plotted. The black line is the prediction of equation 7. Statistical tests indicate no convincing correlation.

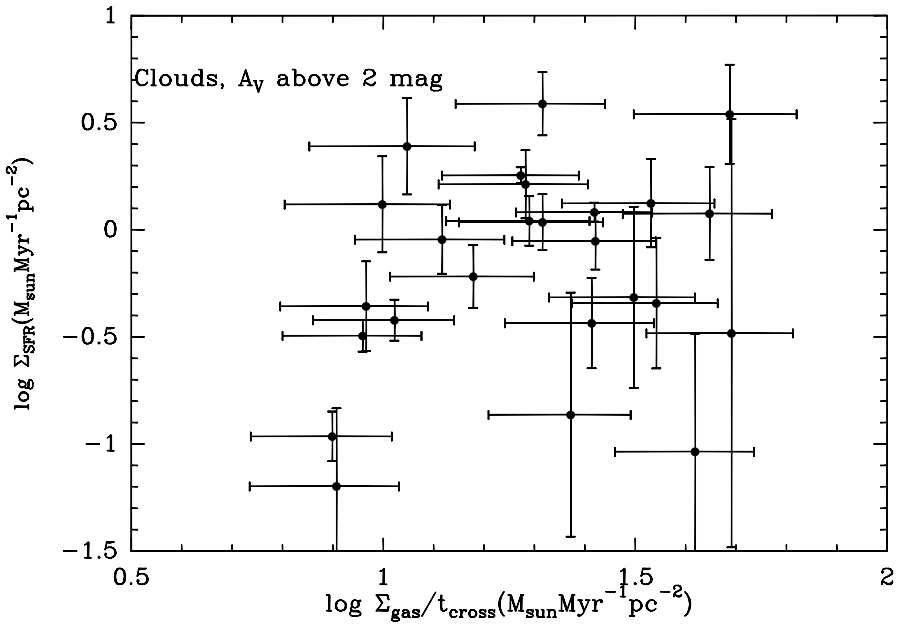

Figure 4. Plot of $\log(\Sigma(\mathrm{SFR}))$ versus $\log(\Sigma_{\mathrm{gas}}/t_{\mathrm{cross}})$ for all YSOs in the nearby clouds. Statistical tests indicate no convincing correlation.

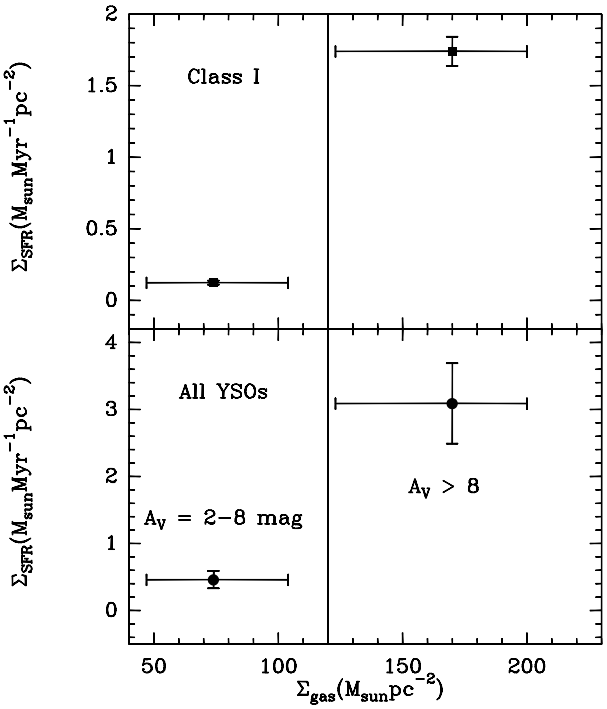

Figure 5. Plot of mean values of Σ(SFR) versus Σ_{gas} for all YSOs in the nearby clouds (lower). In the upper panel, only the Class I YSOs are included. The vertical line is at $\Sigma_{gas} = 120$ $M_\odot$ pc^{-2}, with the conversion from A_V to Σ_{gas} adopted here.

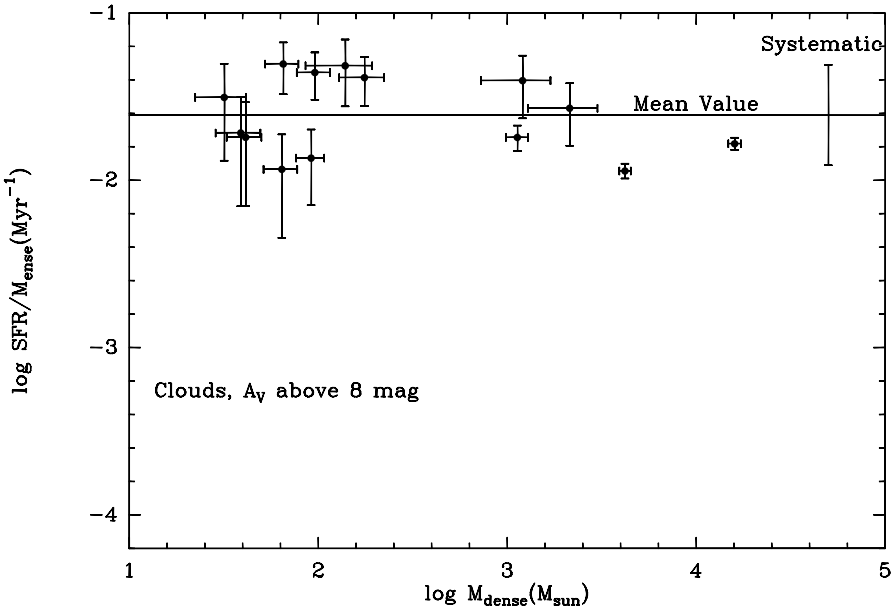

Figure 6. Plot of the logarithm of the SFR per mass of dense gas versus the logarithm of the mass of dense gas. The points are from the nearby clouds counting YSOs and mass at $A_V \geq 8$ mag. The line is the mean value, and the error bars at 4.5 on the abscissa indicate plausible uncertainties of the individual points. The plot scale is the same as for Fig. 7.

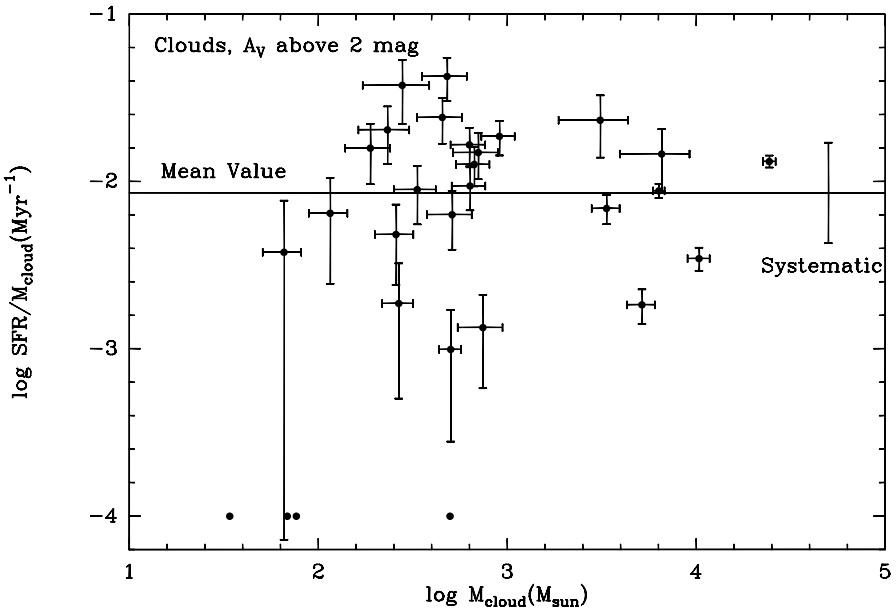

Figure 7. Plot of the logarithm of the SFR per total mass of the cloud versus the logarithm of the total cloud mass. The points are from the nearby clouds counting YSOs. The points plotted at -4.0 on the y-axis have no YSOs, and their location on the y axis is arbitrary. The line is the mean value, and the error bars at 4.5 on the abscissa indicate plausible systematic uncertainties.

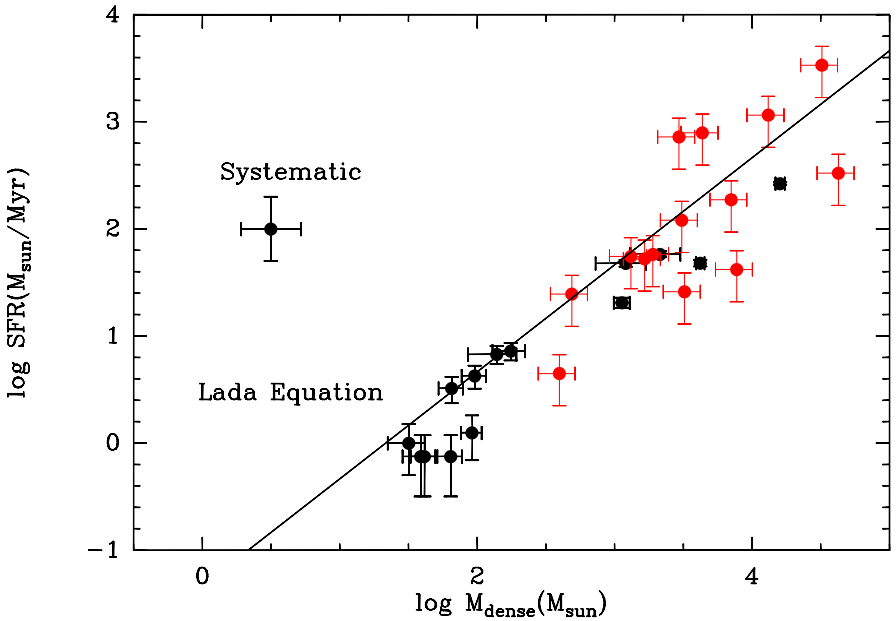

Figure 8. Plot of the logarithm of the SFR in the dense gas versus the logarithm of the mass of dense gas. The black points are from the nearby clouds counting YSOs and mass at $A_V \geq 8$ mag. The red points are from massive dense clumps with SFR from radio continuum and mass of dense gas as the virial mass measured by HCN $J = 1 \rightarrow 0$ emission. The line is the prediction from Lada et al. (2012).